International Journal of
Turbomachinery
Propulsion and Power

MDPI

Article

Performance Evaluation in a Fully Purged High-Pressure Turbine Stage Using Seed Gas Concentration Measurements †

Filippo Merli, Nicolas Krajnc, Asim Hafizovic and Emil Göttlich *

Institute of Thermal Turbomachinery and Machine Dynamics, Graz University of Technology, Inffeldgasse 25A, 8010 Graz, Austria

* Correspondence: emil.goettlich@tugraz.at

† This manuscript is an extended version of the ETC2023-268 meeting paper in the Proceedings of the 15th European Turbomachinery Conference, Budapest, Hungary, 24–28 April 2023.

Abstract: The efficiency assessment of a high-pressure turbine (HPT) stage is complicated by the presence of upstream and downstream purge flows. In fact, the efficiency calculation is often based on mass flow-averaged values of total temperature at the stage inlet and outlet planes. Moreover, the purge flow distribution in the annulus is usually unknown and therefore assumed to be uniform. This paper presents and applies an alternative method to calculate the efficiency of a fully purged HPT stage. Such a definition relies on seed gas concentration measurements at the HPT stage outlet plane to determine the outlet purge flow distribution. After comparing the alternative method to the standard definition (based on the assumption of uniform purge) for the nominal purge case, the efficiency variation between the case with nominal purge and the case without purge is investigated.

Keywords: high-pressure; turbine; cavity; purge; rim seal; performance; efficiency; concentration effectiveness; seed gas

Citation: Merli, F.; Krajnc, N.; Hafizovic, A.; Göttlich, E. Performance Evaluation in a Fully Purged High-Pressure Turbine Stage Using Seed Gas Concentration Measurements. *Int. J. Turbomach. Propuls. Power* **2023**, *8*, 22. https://doi.org/10.3390/ijtpp8030022

Academic Editor: Antoine Dazin

Received: 12 June 2023
Revised: 16 June 2023
Accepted: 10 July 2023
Published: 17 July 2023

1. Introduction

Efficiency is one of the most important parameters characterizing the performance of a turbine stage, given its direct relation to the amount of extractable power from the flow. When the performance investigation concerns High-Pressure Turbine (HPT) stages, the systematic injection of cooling flows (both from the airfoil surfaces and the stator-rotor cavities) complicates the definition of the stage efficiency, generating ambiguities in the actual and ideal power calculations. Numerous efficiency formulations are available in the open literature. Hartsel [1] proposed a first adaptation of the blade row efficiency definition to account for the presence of cooling flows. Young and Horlock [2] developed around Hartsel's definition, suggesting new versions of the ideal power to better represent the maximum achievable output. Berdanier [3] used a formulation that takes into account the cooling flow distribution at the turbine outlet, thanks to coolant effectiveness data. No matter which definition is adopted, studies about efficiency with stator-rotor cavities mainly focus on the (rotor-) upstream hub purge effect in a 1–1.5 HPT stage. Ong et al. [4] and Jenny et al. [5] described an intensification of the hub rotor passage vortex with increased purge mass flow, combined with a radial migration of this feature towards midspan. Such a phenomenon is generally associated with an efficiency drop; Regina et al. [6] quantified it as −0.8% on the total-to-total isentropic stage efficiency per percent of injected cavity mass flow. Additionally, Dahlqvist and Fridh [7] suggested an analytical expression for the entropy generation due to purge and mainstream flow mixing. There are very few works available involving more or different cavities than the upstream hub one; for instance, Zlatinov et al. [8] numerically studied the effect of the upstream shroud purge injection, concluding that it was partially recovering the associated losses by inhibiting the tip leakage flow. Also, Merli et al. [9] experimentally investigated the total pressure loss across intermediate turbine ducts, varying the injection rates in a fully purged HPT stage. A

thorough review of the open literature yielded no publications regarding the performance of a fully purged HPT stage. This paper aims to fill the gap by analyzing a state-of-the-art HPT stage; integrated into a two-stage, dual-spool test setup. Furthermore, the authors would like to provide the engine designers with an appropriate performance parameter and useful insights into the local effects of stator-rotor cavity cooling. At the beginning of the paper, the experimental setup and the measurement techniques are described. Then, an efficiency definition is introduced, which takes into account the purge distribution after it reaches the annulus. After that, the outcome of the mentioned definition is examined and compared to the standard total-to-total efficiency. Finally, the performance discrepancy between the nominal purge case and the no purge case is assessed. This manuscript is an extended version of the ETC2023-268 meeting paper, published in the Proceedings of the 15th European Turbomachinery Conference, Budapest, Hungary, 24–28 April 2023 [10].

2. Experimental Setup

2.1. Transonic Test Turbine Facility (TTTF)

The experimental data were all obtained in the Transonic Test Turbine Facility (TTTF) at the Institute of Thermal Turbomachinery and Machine Dynamics (ITTM, Graz University of Technology). A scheme of the facility is shown in Figure 1. The test section consists of two independent rotor shafts (HPT and LPT), and it is primarily supplied by a 3 MW compressor station (CS1) in an open circuit configuration. Both shafts are overhanging to facilitate maintenance operations. Furthermore, the entire LPT frame can move axially, allowing for flexibility in the turbine design and simplified access to the rotors during the assembly and disassembly phases. The HPT shaft drives a three-stage radial brake compressor (BC), which provides additional mass flow to the test rig up to a maximum of 22 kg/s and 4 bar, while the power extracted at the LPT shaft is dissipated in a 700 kW water brake (WB). The 560 kW suction blower (SB) at the LPT outlet extends the achievable overall pressure ratio and decouples the turbine exit pressure from ambient pressure oscillations. More details about the TTTF can be found in Neumayer et al. [11] and Hubinka et al. [12].

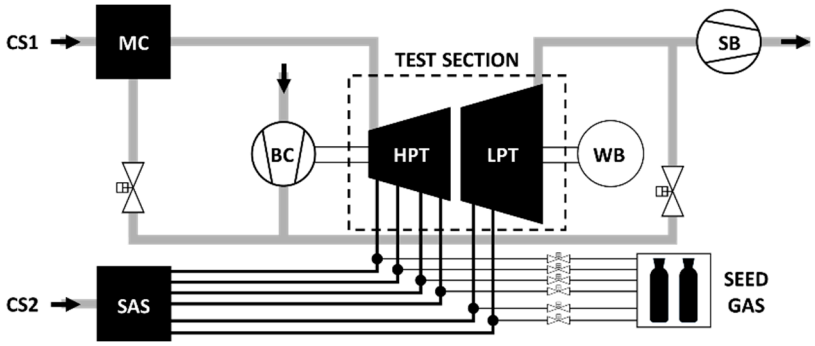

Figure 1. TTTF Layout.

To achieve engine-representative conditions in terms of rotor-stator cavity purge flows, a secondary air system (SAS) was introduced in 2015 (see Steiner et al. [13]). The SAS is supplied by a 1.1 MW electric compressor station (CS2). The secondary air, up to 2.5 kg/s and 12 bar, is split into a cooled and an uncooled strand, feeding two separate reservoirs. A set of servo control valves allows the operator to independently draw the desired ratio of hot and cold air into each cavity line, thus fixing the required purge temperatures and mass flows. As introduced by Patinios et al. [14], the SAS was upgraded in 2019 to enable the injection of tracing gases in the purge lines for concentration measurements. Two pressurized vessels, containing CO_2 and N_2O, respectively, are connected to the purge lines via remotely actuated control valves so that each line can be seeded with the desired concentration of one of those gases.

2.2. Test Vehicle and Operating Conditions

The test setup considered for this study is a two-stage turbine, with the cross-section and meridional view reported in Figure 2. It is constituted by an HPT stage, an intermediate turbine duct with turning vanes and splitter, called the Turbine Vane Frame (TVF), and an LPT counter-rotating blade row. The arrangement is representative of the last HPT stage and first LPT stage in a state-of-the-art turbofan engine, and it includes six purged stator-rotor cavities: four in the HPT stage and two in the LPT stage. The HPT and LPT hub cavities are engine-relevant radial-clearance rim seals, while the shroud cavities are circumferentially continuous axial slots. Out of the whole assembly depicted in Figure 2, this investigation focuses its attention on the HPT side, in particular on the blue, dash-contoured control volume. The control volume is bounded radially by the position of the HPT cavity instrumentation and axially by two $r - \vartheta$ measurement planes: the HPT inlet plane (Plane A) and the HPT outlet plane (Plane B). The detailed description of the measurement apparatus in the control volume is postponed to the Section 3.

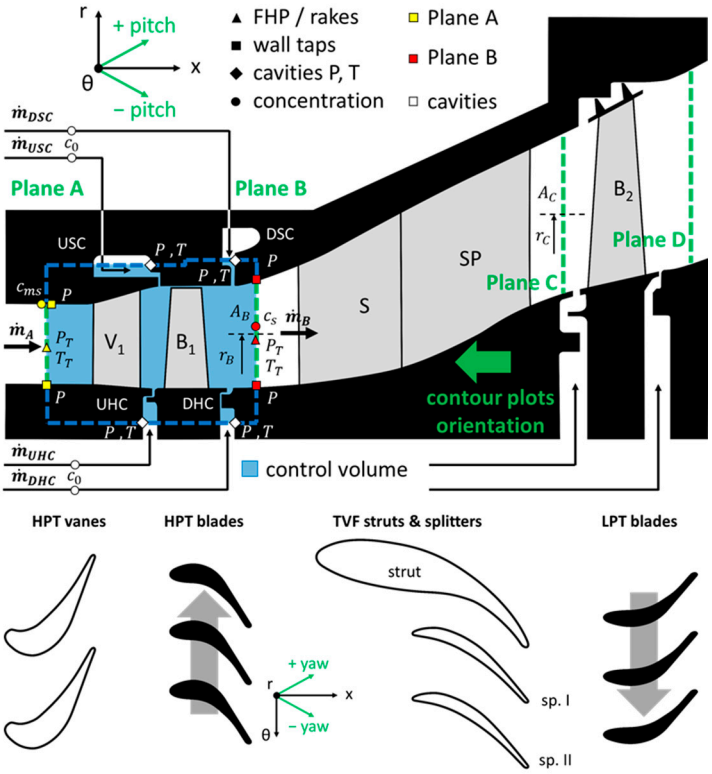

Figure 2. Test vehicle cross-section and meridional view.

The nominal operating conditions, namely the HPT total pressure ratio, the HPT exit Mach number, the TVF Reynolds number, and the HPT purge mass flows, are illustrated in Table 1 (some are given as broad intervals due to confidentiality reasons). Concerning the purge mass flows, they are expressed as fractions of the UHC supply, which is in the range $(0.5\% - 1\%)\dot{m}_A$. In addition to the nominal case, an off-design case was tested, which is obtained by switching off the HPT purge supply while keeping the other parameters in Table 1 unchanged. Throughout the rest of the paper, the nominal case will be referred to as PFR 100% and the case without HPT purge as PFR 0%, where the Purge Flow Ratio is defined as $PFR = \dot{m}_{purge}/\dot{m}_{purge,nominal}$. Finally, it should be mentioned that the LPT cavities are also fed with purge air, and their supply is kept the same during PFR 0% and PFR 100% measurements.

Table 1. Test vehicle nominal operating conditions (PFR 100%) for annulus and cavity flows.

Annulus Flow	Value	Purge Flow	$\dot{m}_{purge}/\dot{m}_{UHC}$ [%]
$P_{T,A}/P_{T,B}$ [−]	$2-2.5$	Upstream Hub (UHC)	100
M_B [−]	0.5	Upstream Shroud (USC)	77
α_B [°]	$0-5$	Downstream Hub (DHC)	102
$Re_B = (\rho v/\mu)_B L_{B-C}$ [−]	1.7×10^6	Downstream Shroud (DSC)	113

3. Measurement Techniques

3.1. Aerodynamic Measurements

The aerodynamic measurements are performed to retrieve pressure, temperature and mass flow values at the HPT stage inlet (Plane A), at the HPT stage outlet (Plane B), and inside the HPT cavities.

In Plane A, the total pressure and the total temperature are acquired by two Kiel-head rakes. The rakes were designed at the ITTM, and they have six equispaced heads each, with an angle of 90° from the radial stem and 0° from the axial direction. The total pressure heads are connected to a NetScanner 9116 Pressure Scanner, while the type K thermocouples in the temperature heads are connected to a NI 9214 Temperature Input Module. For each pressure and temperature head, 30 values are acquired at a sampling frequency of 5 Hz and then averaged, with a final combined uncertainty of ±5 mbar and ±1 K, respectively. Both rakes are traversable across the full 360° extent; however, the circumferential uniformity of the inlet flow, evaluated in a different test campaign, allowed to measure the radial profiles at a fixed location, with a deviation from the circumferentially averaged profiles within the uncertainty of the instruments. In order to capture the steep gradients in the near-endwall flow, the P_T rake profile is integrated with data from boundary layer rakes (hub and shroud, six heads each), as well as wall taps (hub and shroud, seven taps each). On the other hand, the endwall temperature is assumed to be equal to the mixing chamber temperature (MC in Figure 1), due to the thermal conduction between the casings. The resulting radial profiles $P_{T,A}(r)$ and $T_{T,A}(r)$ are represented in Figure 3a for the PFR 100% case.

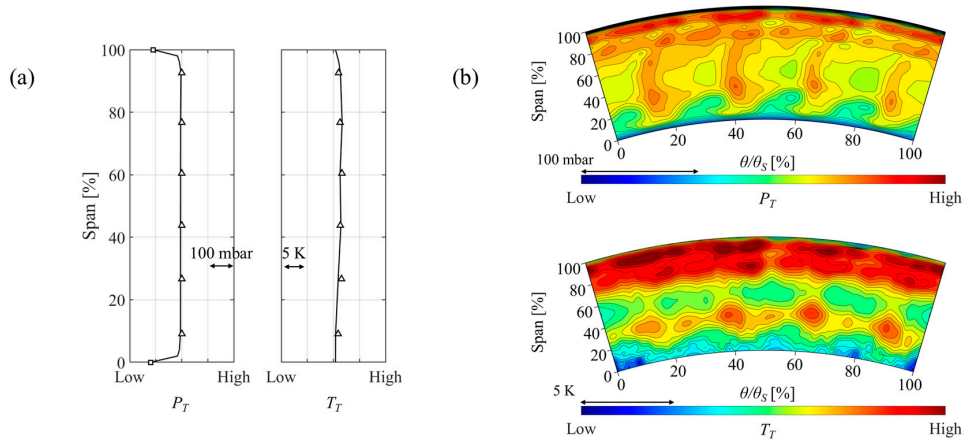

Figure 3. Aerodynamic measurements: (**a**) P_T and T_T radial profiles in Plane A. The triangles and squares indicate the position of rake heads and wall pressure taps, respectively; (**b**) P_T and T_T contour plots in Plane B.

Plane B total pressure and total temperature are acquired with a Five-Hole Probe (FHP). The FHP was manufactured and calibrated at the Institute of Jet Propulsion and Turbomachinery (RWTH Aachen University). The head is inclined 90° from the stem axis and is integrated with a shielded, calibrated type K thermocouple. The 30 values at 5 Hz for each measurement point are acquired with a NetScanner 9116 Pressure Scanner (pressure lines) and a NI 9214 Temperature Input Module (thermocouple), for a combined uncertainty of ±3 mbar and ±0.8 K, respectively. During the experimental tests, the probe

is traversed across a 20 × 60 measurement grid (radial × tangential), which covers a 1 TVF pitch and approximately 90% of the channel height in Plane B. The P_T data from the FHP is complemented by boundary layer rakes readings (hub and shroud rakes, six heads each) and wall taps (hub and shroud walls, seven taps each), while the T_T boundary layer profile is obtained from a RANS simulation of the HPT stage using experimental boundary conditions. The resulting $P_{T,B}(r,\theta)$ and $T_{T,B}(r,\theta)$ contour plots are depicted in Figure 3b.

The pressure and temperature values inside the HPT cavities are acquired with a set of three wall taps and three type K thermocouples, uniformly spaced across the circumference at the radial positions displayed in Figure 2. The acquisition procedure (number of values, sampling rate and acquisition modules) is the same as the one described for the other planes. The estimated uncertainty is ±5 mbar for pressure measurements and ±1 K for temperature measurements.

Finally, the main mass flow and the purge mass flow are measured upstream of the test section: the former is the sum of the readings from two Venturi flow meters (±2%), placed at the exit of the compressor station and brake compressor (see Figure 1); the latter are measured with McCrometer V-Cone Flow Meters (±0.5%), one on every purge supply line. It is also worth mentioning that all the aerodynamic measurements described in this section are taken within a single test run to avoid the application of day-to-day corrections to the dataset.

3.2. Concentration Measurements

Seed gas concentration measurements are performed to characterize the HPT purge flow distribution at the outlet of the HPT stage. The technique consists of the following steps: A certain mass of tracing gas is fed to one of the purge supply lines to reach the desired concentration in the stator-rotor cavity ($c_0 \approx 5\%_{vol.}$ in this study) The preexisting concentration of tracing gas in the unseeded mainstream flow c_{ms} is acquired, as well as the concentration c_s in the location of interest (i.e., Plane B). Finally, the purge flow effectiveness is calculated with:

$$\varepsilon(r,\theta) = \frac{c_s(r,\theta) - c_{ms}}{c_0 - c_{ms}}, \tag{1}$$

where (r,θ) indicates each point of the 2D measurement grid in Plane B. With reference to Equation (1), $\varepsilon = 0$ indicates that no trace of purge flow is present in the analyzed sample; $\varepsilon = 1$ indicates that the sample is completely constituted by purge gas; and $0 < \varepsilon < 1$ indicates that the sample is a mixture of mainstream and purge gas. During the test campaign, c_{ms} was sampled through one of the heads of the Plane A shroud boundary layer rake, while $c_s(r,\theta)$ is obtained by traversing a pitot probe across the same Plane B annulus sector covered by the FHP. The concentration values are measured with a Siemens Ultramat 6E gas analyzer. Such devices are dual-gas (CO_2, N_2O), meaning that two cavities can be seeded in the same test run and the two corresponding $\varepsilon(r,\theta)$ fields can be retrieved from the same set of samples. The estimated uncertainty for the resulting effectiveness values is ±0.003.

After applying the described procedure to all the cavities, the combined effectiveness is calculated as follows: $\varepsilon_c = \varepsilon_{UHC} + \varepsilon_{USC} + \varepsilon_{DHC} + \varepsilon_{DSC}$ and its contour plot is shown in Figure 4. A thorough interpretation of the rotor upstream and downstream purge distribution in Plane B is available in Merli et al. [15]; for the sake of this work, it is important to underline that the downstream purge is responsible for the high-effectiveness bands at Span > 90% and Span < 10% ($\varepsilon_{c,max} \approx 0.2$), while the upstream purge is entrained in the rotor secondary structures, therefore it is far more diluted with mainstream flow ($\varepsilon_{UHC+USC} \ll \varepsilon_{DHC+DSC}$) and it spreads across a larger portion of the annulus (Span > 60% and Span < 40%).

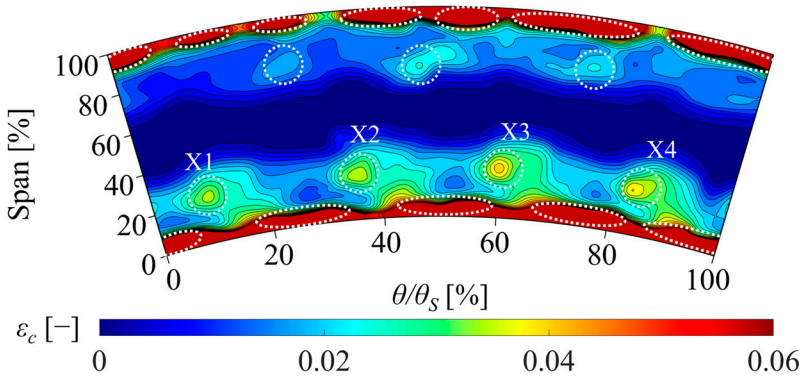

Figure 4. Plane B combined effectiveness ε_c contour plot.

4. Methodology

The Section 4 first presents the definitions of efficiency utilized in this study. The terminology adopted in such definitions refers to Figure 2. After that, the strategy for the efficiency uncertainty calculation is explained.

4.1. Efficiency Calculation

The turbine efficiency is usually intended as the ratio between actual power output and a hypothetical ideal power extracted from the working gas:

$$\eta = \frac{P_{real}}{P_{ideal}}, \quad P_{real} = P_{real,ad} + P_{heat} = P_{shaft} + P_{mech} + P_{windage} + P_{heat}, \tag{2}$$

where P_{heat} is the power dissipated through heat transfer in a nonadiabatic stage; P_{shaft} is the net power delivered at the shaft; P_{mech} is the power loss in the mechanical elements (e.g., bearings); and $P_{windage}$ is the power loss due to friction inside the rotor-stator cavities. For an adiabatic, uncooled stage inside a multistage turbine arrangement, the total-to-total adiabatic efficiency is normally adopted.

$$\eta_{TT} = \frac{P_{real,ad}}{P_{ideal}} = \frac{h_{T,inlet} - h_{T,outlet}}{h_{T,inlet} - h_{T,is,\ outlet}}. \tag{3}$$

Now, it should be clarified that the tested turbine is not adiabatic; however, the present work aims to compare different efficiency definitions and operating conditions rather than providing absolute efficiency values. Additionally, the mentioned conditions only differ in terms of PFR, i.e., in terms of a relatively small amount of mass flow. On such grounds, P_{mech}, $P_{windage}$ and P_{heat} are assumed to be unaltered among the analyzed cases and thus not considered in the efficiency calculation.

4.1.1. Turbine Efficiency–Based on Uniform Purge Assumption (UP)

Applying the same approach behind Hartsel's cooled blade-row efficiency (see Hartsel [1]) to Equation (3), the well-known total-to-total efficiency for cooled stages is obtained:

$$\eta_{\mathrm{UP}}(r,\theta) = \frac{\dot{m}_A\left[\overline{h_{T,A}} - h_{T,B}(r,\theta)\right] + \sum_{k=UHC,\ldots,DSC} \dot{m}_k\left[\overline{h_k} - h_{T,B}(r,\theta)\right]}{\dot{m}_A\left[\overline{h_{T,A}} - h_{T,is,B}(r,\theta)\right] + \sum_{k=UHC,\ldots,DSC} \dot{m}_k\left[\overline{h_k} - h_{k,is,B}(r,\theta)\right]}, \tag{4}$$

where $h_{k,is,B}$ derives from the isentropic, unmixed expansion of the purge flows from their initial supply conditions (inside cavities UHC, USC, DHC and DSC) to the Plane B total pressure. It should be noted that, while Plane B is represented by 2D enthalpy fields, it is not possible to have the same characterization for the main flow and purge flow inlet terms, at least without first performing particle tracking through the HPT stage. For this reason, $\overline{h_{T,A}}$ and $\overline{h_k}$ are averaged scalar values. To avoid the perfect gas approximation

$\Delta h_{T,A-B} = \bar{c}_{P,A-B}\Delta T_{T,A-B}$, which leads to important errors on c_P for the large temperature drops in the tested turbine, enthalpies are calculated using the dry air properties from the CoolProp free digital library (Bell et al. [16]). Given two thermodynamic values, the software can return the other properties of the desired gas, for example, $h_{T,B} = f(P_{T,B}, T_{T,B})$ and $h_{T,is,B} = f(P_{T,B}, s_A)$.

The fundamental limitation of the uniform purge assumption (UP) is that the overall mass flows $\dot{m}_A$ and $\dot{m}_k$ are associated with the enthalpy drop at each (r, θ) point. In other words, the main mass flow and the purge mass flow are assumed to be fully mixed across the measured sector. Such an approximation, which is far from true in real engine HPT stages, is necessary where no information about the purge flow distribution in the annulus is available.

4.1.2. Turbine Efficiency–Based on Measured Purge Distribution (PD)

When the 2D purge flow distribution at the HPT outlet is experimentally or numerically assessed, the mass flow associated with each measured point of Plane B can be separated into multiple contributors: the fraction coming from Plane A main flow, which undergoes the enthalpy drop $\left(\overline{h_{T,A}} - h_{T,B}\right)$; the k fractions coming from the HPT cavities, which experience the drop $\left(\overline{h_k} - h_{T,B}\right)$. This leads to the efficiency definition of Equation (5), based on the measured purge distribution (PD):

$$\eta_{\mathrm{PD}}(r,\theta) = \frac{\dot{m}_A(r,\theta)\left[\overline{h_{T,A}} - h_{T,B}(r,\theta)\right] + \sum_k \dot{m}_k(r,\theta)\left[\overline{h_k} - h_{T,B}(r,\theta)\right]}{\dot{m}_A(r,\theta)\left[\overline{h_{T,A}} - h_{T,is,B}(r,\theta)\right] + \sum_k \dot{m}_k(r,\theta)\left[\overline{h_k} - h_{k,is,B}(r,\theta)\right]}, \tag{5}$$

where $\dot{m}_A(r,\theta)$ and $\dot{m}_k(r,\theta)$ have to fulfill the mass balance for each measurement point and, in turn, the overall mass balance:

$$\dot{m}_B(r,\theta) = \dot{m}_A(r,\theta) + \Sigma_k \dot{m}_k(r,\theta) \quad \overset{\Sigma_i \Sigma_j}{\rightarrow} \quad \dot{m}_B = \dot{m}_A + \Sigma_k \dot{m}_k. \tag{6}$$

In this case, $\dot{m}_B(r,\theta) = (\rho v \Delta A)(r,\theta)$ is determined using the FHP results, while for $\dot{m}_k(r,\theta)$ it is assumed that $\varepsilon_{c,k}(r,\theta) \approx x_k(r,\theta) = \dot{m}_k(r,\theta)/\dot{m}_B(r,\theta)$, i.e., that the purge effectiveness is analogous to the purge mass fraction in the annulus (the density effect is considered negligible). $\dot{m}_A(r,\theta)$ can be then calculated as $\dot{m}_B(r,\theta) - \Sigma_k \dot{m}_k(r,\theta)$.

A similar approach to the efficiency calculation has been proposed by Berdanier [3]. In that work, 1D total pressure and total temperature rake data are utilized both at the HPT stage inlet and outlet. Moreover, the effectiveness profiles are borrowed from a different turbine stage. To the best of the authors' knowledge, this is the first publication involving a full 2D FHP dataset at the HPT stage outlet, also combined with a full 2D effectiveness distribution measured in the same plane.

Finally, in the scenario without purge (PFR 0%), both η_{UP} and η_{PD} collapse into the same equation, analogous to Equation (3):

$$\eta_{\mathrm{PFR\ 0\%}}(r,\theta) = \frac{\dot{m}_A\left[\overline{h_{T,A}} - h_{T,B}(r,\theta)\right]}{\dot{m}_A\left[\overline{h_{T,A}} - h_{k,is,B}(r,\theta)\right]}. \tag{7}$$

4.2. Efficiency Calculation

It is common practice in engineering applications to assess the uncertainty $U_Y = \pm\sigma_Y$ of a derived variable $Y = f(X_1, \ldots, X_n)$ by means of (see for example Holman [17])

$$\sigma_Y = \sqrt{\sum_{m=1}^{n}\left(\frac{\partial f}{\partial X_m}\sigma_{X_m}\right)^2}. \tag{8}$$

In the case of the analyzed HPT stage, $\eta = f(P_{T,A}, T_{T,A}, P_{T,B}, T_{T,B}, P_k, T_k, \dot{m}_B, \dot{m}_k)$. The large number of variables involved and their non-linear dependencies make the evaluation of the partial derivatives rather cumbersome. The uncertainty is therefore calculated numerically through a result perturbation approach: $\Delta Y_m = f(X_1, \ldots, X_m, \ldots, X_n) - f(X_1, \ldots, X_m + \sigma_{X_m}, \ldots, X_n)$ is calculated for each X_m variable and, assuming that $\partial f / \partial X_m \approx \Delta Y_m / \sigma_{X_m}$, the standard deviation becomes

$$\sigma_Y \approx \sqrt{\sum_{m=1}^{n} \Delta Y_m{}^2}. \tag{9}$$

An analogous application of the result perturbation process to the evaluation of an HPT stage efficiency uncertainty can be found in Dénos et al. [18]. The resulting efficiency uncertainty is $U_\eta = \pm 1.28\%$ for the PFR 100% case with the PD definition. A sensitivity analysis revealed that $T_{T,B}$ and $T_{T,A}$ have the highest effect on the uncertainty, followed by $P_{T,B}$ and $P_{T,A}$, while the impact of the purge-related quantities is negligible.

5. Results and Discussion

The Section 5 is divided into three sub-sections: in the first one, the 2D map of the PD efficiency is investigated; in the second one, the outcome of the PD and UP efficiency definitions is compared; and in the third one, the effect of the purge mass flow variation on the HPT stage efficiency is described. The charts and contour plots presented below are built by interpolating the experimental values, reported in the charts as white triangles (FHP), on a finer grid to improve rendering and pattern recognition. The interpolated grid has 0.1° circumferential and 0.1 mm radial steps, while the interpolation algorithm is MATLAB's Modified Akima cubic scheme.

5.1. HPT Stage Efficiency 2D Map

Figure 5 represents the contour plot of PD efficiency, calculated through Equation (5) for the PFR 100% case. The superposed black dashed lines, reported by Merli et al. [15], isolate regions of strongly positive and strongly negative streamwise vorticity in order to understand the impact of the HPT secondary structures on the efficiency map. A high-efficiency circumferential band is located around midspan, between 40% and 70% of the Span; in this core region, the flow is affected the least by the HPT secondary vortices, thus the extracted work is higher. On the other hand, the adjacent bands (20–40% Span and 70–80% Span) appear as regions of low efficiency, with a max-to-min efficiency drop of up to 10 pts between core flow and adjacent bands. In fact, such regions are affected by the HPT rotor's Lower Passage Vortex (LPV_{B1}) and Upper Passage Vortex (UPV_{B1}), which are known to be detrimental to the turbine's performance. For Span > 80%, the efficiency remains low with respect to the core flow; this is ascribed to the hot (see Figure 3b), undeflected Tip Leakage Flow (TLF) between 80% and 90% Span and to the associated Scraping Vortex (SV) at Span > 90%. It is interesting to notice how the LPV_{B1}, UPV_{B1} and TLF bands are not circumferentially uniform, as one would expect from rotating structures investigated with steady-state techniques, but they show a lobed pattern. The reason behind it is the downstream influence of the HPT vanes, which modulate the rotor-related features in a circumferential direction. A clear example of the stator effect is visible below the 20% Span, where the white dotted circles indicate the location of the vanes of the Lower Passage Vortices (LPV_{V1}) at $\theta/\theta_S \approx 25\%$, 50%, 75% and 90%. Finally, the combined analysis of Figures 4 and 5 shows that the purge-rich flow is generally delivering lower efficiency values compared to the undiluted mainstream flow; the white dotted circles are located at the same positions in both plots, revealing that local effectiveness maxima are in fact coupled with local efficiency minima. As discussed in the Section 1, this connection has been observed before in partially purged turbines (UHC purge only), and it is hereby validated for a fully purge turbine as well.

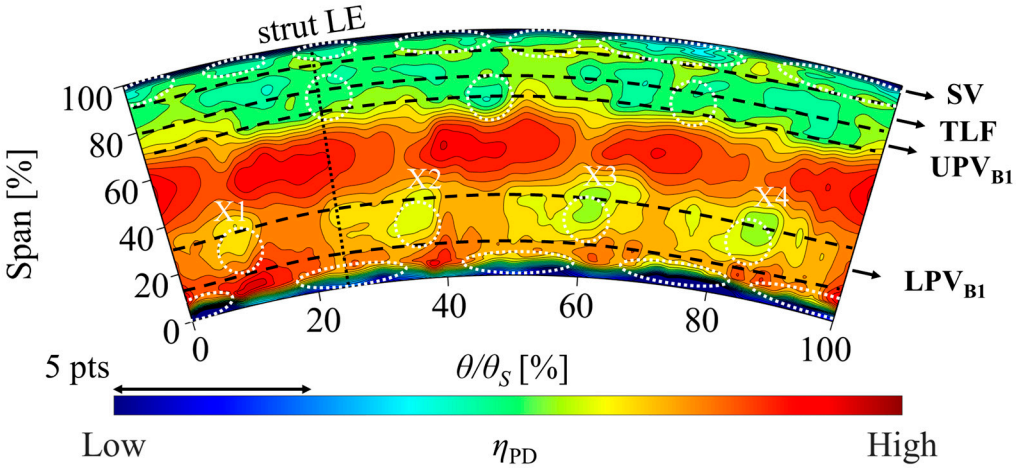

Figure 5. PD efficiency η_{PD} contour plot for the PFR 100% case.

5.2. Efficiency Definition Effect

Further insight into the relationship among purge distribution, secondary flows and efficiency can be retrieved from the discussion of Figure 6. Figure 6a represents the mass-averaged radial profiles of η_{PD} (black solid line) and η_{UP} (black dashed line) for the PFR 100% case, as per Equations (4) and (5), respectively. Additionally, the area-averaged radial profile of ε_c (grey solid line) and the radial position of the secondary flows are depicted. The local differences between η_{PD} and η_{UP} are substantial, with peaks above 1 pt. The highest deviations are located in the core flow region, where $\varepsilon_c \approx 0$, as well as for Span > 90% and Span < 10%, where ε_c is high due to the significant presence of downstream purge. This behavior, also discussed by Berdanier [3], is associated with the different interpretations of the Plane A–Plane B enthalpy drop depending on the local purge flow content. In order to better explain such a concept, the fully mixed effectiveness $\varepsilon_{c,fm} = \varepsilon_{UHC,fm} + \varepsilon_{USC,fm} + \varepsilon_{DHC,fm} + \varepsilon_{DSC,fm}$ is plotted (grey dotted line), where for each cavity k:

$$\varepsilon_{k,fm} = \frac{c_{k,fm} - c_{ms}}{c_0 - c_{ms}}, \quad c_{k,fm} = \frac{\dot{m}_A c_{ms} + \dot{m}_k c_{k,0} + \Sigma_{l=1}^{\text{all cavities}-k} \dot{m}_l c_{ms}}{\dot{m}_A + \Sigma_k \dot{m}_k}. \tag{10}$$

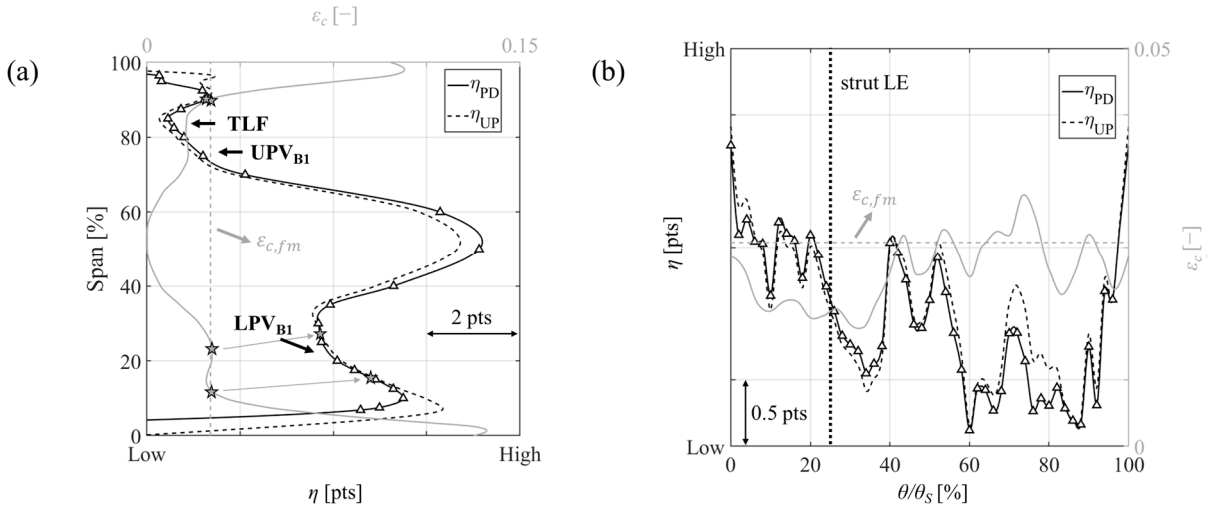

Figure 6. Efficiency definition effect: (**a**) η_{PD}, η_{UP} and ε_c radial profiles; (**b**) η_{PD}, η_{UP} and ε_c circumferential profiles. The triangles represent the FHP measurement grid in Plane B.

The fully mixed effectiveness represents the theoretical condition in which purge flows and annulus flows are perfectly amalgamated, i.e., the purge distribution is uniform across Plane B. By definition, if $\varepsilon_c = \varepsilon_{c,fm}$, then $\eta_{PD} = \eta_{UP}$. The experimental data in Figure 6a show good agreement with this statement: the intercepts between η_{PD} and η_{UP} and between ε_c and $\varepsilon_{c,fm}$ are indicated by grey stars. The slight radial mismatch is ascribed to small purge mass flow variations when the seed gas is injected. In the regions where $\varepsilon_c > \varepsilon_{c,fm}$, η_{PD} takes into account that a higher fraction of the local enthalpy goes into the purge–mainstream flow mixing instead of being converted into power output, thus $\eta_{PD} < \eta_{UP}$ (η_{UP} assumes $\varepsilon_c(r,\theta) = \varepsilon_{c,fm}\ \forall\ r,\theta$). Vice versa, $\eta_{PD} > \eta_{UP}$ where $\varepsilon_c < \varepsilon_{c,fm}$, due to opposite considerations.

Figure 6b shows the mass-averaged circumferential profiles of the same quantities in Figure 6a, preserving colors and line styles. Once again, the highest deviation between η_{PD} and η_{UP} are found when $\varepsilon_c \neq \varepsilon_{c,fm}$, in particular $\eta_{PD} < \eta_{UP}$ if $\varepsilon_c > \varepsilon_{c,fm}$ and $\eta_{PD} > \eta_{UP}$ if $\varepsilon_c < \varepsilon_{c,fm}$, for the same reasons discussed above. It is also noticeable that the segment $10\% < \theta/\theta_S < 40\%$ has lower effectiveness values compared to the symmetric segment $60\% < \theta/\theta_S < 90\%$. The cause is the TVF strut LE potential effect, which produces higher hub pressure at $\theta/\theta_S \approx 25\%$ (black dotted line), reducing the amount of egress flow accumulating there and, in turn, increasing the local efficiency. The same considerations can be qualitatively drawn by looking at Figures 4 and 5, where the lobes X1–X2 have lower effectiveness and higher efficiency than X3–X4. Finally, it should be mentioned that, although the local differences between η_{PD} and η_{UP} are significant, they are only marginally affecting the overall mass-averaged scalar efficiency since $\Delta\eta_{PD-UP} = -0.06\ pts$.

5.3. Purge Flow Variation Effect

Figure 7 displays the efficiency contour plot for the PFR 0% case. The black dashed lines and the white dotted circles indicate the position of the secondary flow structures and of the high-effectiveness spots in the PFR 100% case to help visualize the changes of such features between the two operating conditions. The midspan, high-efficiency core flow region appears to be wider in the case without purge (from 30% Span to 75% Span). The low-efficiency adjacent bands, corresponding to LPV_{B1}-LPV_{V1} and UPV_{B1}-TLF-SV, are instead confined to narrower corridors, closer to the endwalls (Span < 30% and Span > 75%, respectively). Moreover, in the PFR 0% case, the low-efficiency lobes X1–X4 all appear circumferentially shifted against the direction of rotation of the HPT blades due to a yaw angle decrease of about 5° in the region of such flow features, calculated using the FHP data. This is a direct consequence of the HPT purge absence, already observed by Sterzinger et al. [19], at the outlet of a similar stage.

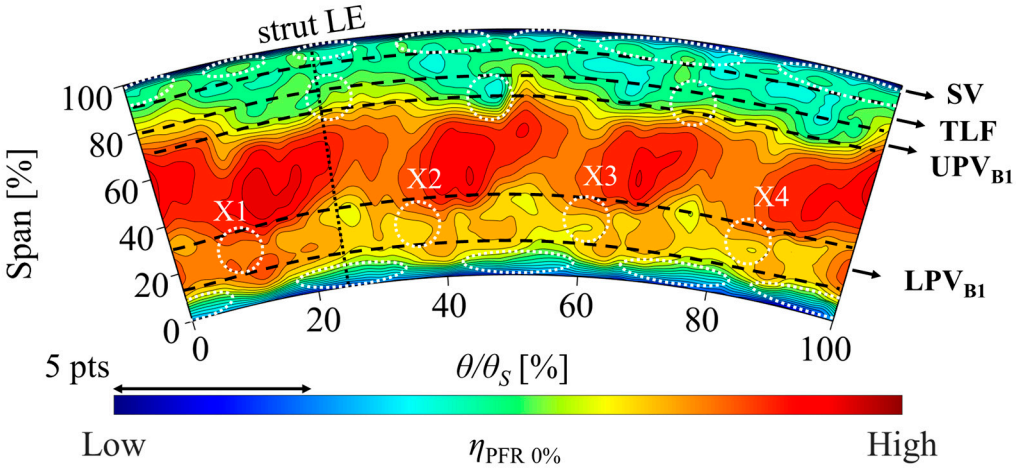

Figure 7. Efficiency contour plot for the PFR 0% case.

For a more quantitative analysis, the mass-averaged radial profiles of $\eta_{PFR\ 100\%}$ and $\eta_{PFR\ 0\%}$ are reported in Figure 8a (black solid lines and black dashed lines, respectively),

together with the radial distribution of $\dot{m}_A/\dot{m}_B$ (grey line). The PD efficiency definition is utilized for $\eta_{\text{PFR 100\%}}$, while η_{PD} and η_{UP} converge into Equation (7) for $\eta_{\text{PFR 0\%}}$. Interestingly, Figure 8a shows that peak core flow efficiency is basically the same for $\eta_{\text{PFR 100\%}}$ and $\eta_{\text{PFR 0\%}}$: the difference lies in the radial extension of the core flow band, unperturbed by LPV_{B1} and UPV_{B1}. In agreement with the existing literature (Regina et al. [6] and Zerobin et al. [20], among others), the upstream hub purge is entrained in LPV_{B1} and UPV_{B1}, intensifying and pushing them toward midspan. In Figure 8a, the LPV_{B1} magnitude and position change between the cases leads to local efficiency deviations up to 2 pts in favor of $\eta_{\text{PFR 0\%}}$, and to a radial offset of about 10% Span. This trend is still recognizable but less pronounced for UPV_{B1}, possibly due to the presence of the TLF, which increases the dilution of the purge air in the annulus gas, smearing out its effect. At the same time, the upstream shroud purge seems to partially suppress the TLF-related losses, producing experimental evidence for the numerical findings of Zlatinov et al. [8]. Finally, it is quite surprising to see that $\Delta\eta_{\text{PFR 100\%}-\text{PFR 0\%}} \approx 1.5\ pts \gg 0$ at approximately 90% Span and 10% Span. This is explained by the action of the downstream purge, which in Plane B is concentrated in the near-endwall regions of the channel (Span > 90% and Span < 10%). In fact, the downstream purge, in combination with the rotor passage vortices radial migration, forces a redistribution of the annulus flow (see the peaks in the $\dot{m}_A/\dot{m}_B$ curve at 15% Span and 85% Span). The outcome is that venae of mainstream, high-performance fluid are enclosed between the rotor passage vortices and the endwalls. Such a phenomenon, clearly recognizable also in Figure 5 at 15% Span, disappears in the absence of purge. The explanation above would also justify why, to the authors' knowledge, such $\Delta\eta > 0$ spots have never been described in the open literature, which mostly focuses on partially purged HPT stages, especially with upstream hub purge only.

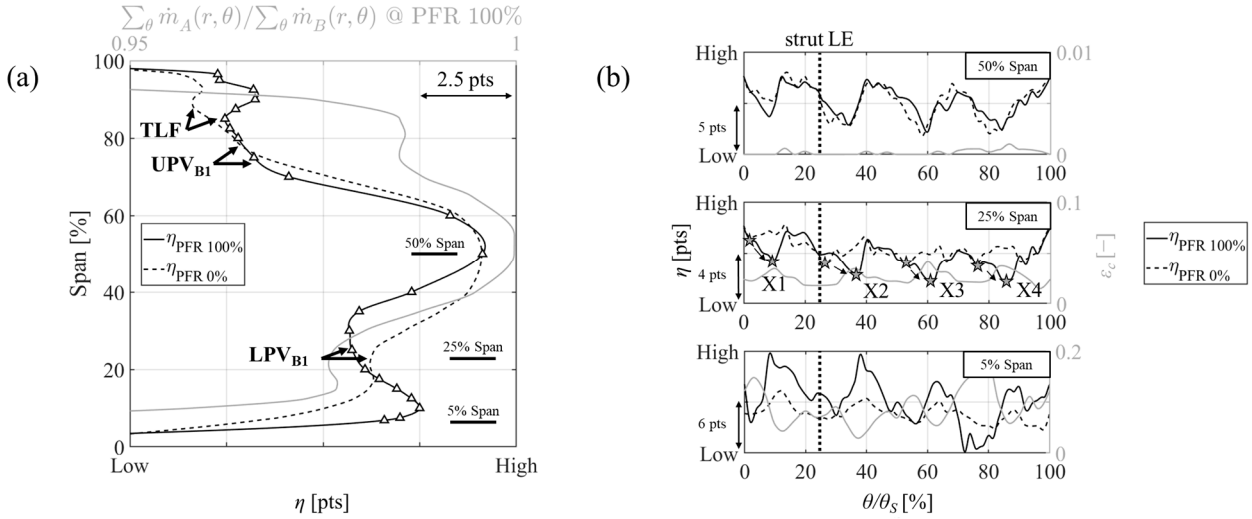

Figure 8. Purge flow variation effect: (**a**) $\eta_{\text{PFR 100\%}}$, $\eta_{\text{PFR 0\%}}$ and $\dot{m}_A/\dot{m}_B$ at PFR 100% radial profiles; (**b**) $\eta_{\text{PFR 100\%}}$, $\eta_{\text{PFR 0\%}}$ and ε_c circumferential profiles at 5%, 25% and 50% Span. The triangles represent the FHP measurement grid in Plane B.

Figure 8b reports the circumferential efficiency profiles for both purge cases at three interesting radial locations: 5% Span, where there is a high concentration of downstream purge; 25% Span, where the upstream purge is transported inside LPV_{B1}; and 50% Span, where almost no cooling air is detected. The grey line in each plot represents the ε_c profile at the corresponding radial position. At 5% Span, $\eta_{\text{PFR 100\%}}$ follows a sinusoidal behavior, in phase opposition with the effectiveness profile and with larger spatial oscillations compared to the $\eta_{\text{PFR 0\%}}$ case. The trend is produced by the HPT vanes since their hub pressure distribution circumferentially clocks the upstream purge egress, thus affecting the efficiency. However, a second contribution is visible in the form of a higher $\eta_{\text{PFR 100\%}}$ mean value in the segment $0\% < \theta/\theta_S < 50\%$, which is caused by the already described potential field of

the TVF strut LE (black dotted line), which locally reduces the downstream purge egress. At 25% Span, the sinusoidal trend of $\eta_{\text{PFR 100\%}}$ persists, but the fluctuations have lower intensity and more circumferential uniformity. In fact, the location is mostly influenced by the upstream hub coolant flow, whose egress and distribution are less affected by the TVF strut. In addition, the local $\eta_{\text{PFR 100\%}}$ and $\eta_{\text{PFR 0\%}}$ minima indicated with grey stars show the circumferential shift of the peaks X1–X4, also noticed in Figure 7. To conclude, at 50% Span, the effectiveness values are low; therefore, the PFR 100% and PFR 0% lines are practically superposed, showing a very good match.

6. Conclusions

The paper investigates the performance of a fully purged HPT stage operating in a dual-spool, engine-representative configuration. An alternative definition (PD) of the total-to-total adiabatic stage efficiency is proposed, which takes into account the HPT purge distribution at the stage outlet, calculated using dual tracing gas concentration measurements. Such a definition is compared to the standard Hartsel-based formulation (UP). The UP efficiency is found to underestimate the stage performance in the core flow, where the purge effectiveness values are below the fully mixed threshold, compared to the PD version. At the same time, the UP definition overestimates the performance of the purge-rich flows because it underpredicts the amount of energy lost in the mixing process. Finally, the PFR 100% case efficiency is compared to one of the PFR 0% cases. The upstream purge is entrained in the rotor passage vortices, magnifying their losses (local differences up to 2 pts in the radial profiles) and shifting them towards midspan (10% Span offset for LPV_{B1}). However, the additional losses of the shroud purge are mitigated by the partial suppression of the TLF. On the other hand, the downstream purge, collected in thin layers next to the endwalls, is responsible for a mass flow redistribution that traps streaks of high-efficiency annulus flow between the rotor passage vortices and the walls. The circumferential distribution in the lower half of the HPT stage outlet plane shows that, in the near-endwall region, rich in downstream purge air, the potential effect of the strut leading edge is beneficial for the efficiency, locally reducing the coolant egress; already at 25% Span, the effect of the strut is negligible, while the HPT vanes downstream propagation are determining the effectiveness maxima (i.e., the efficiency minima).

The authors argue that the PD efficiency better represents the flow physics inside the turbine stage, with deviations between mass-averaged radial profiles of the PD and UP efficiencies up to 1 pts. If the local deviations are remarkable, it should be noted that the overall scalar efficiency values do not appear significantly different. The main drawback of the proposed method is that additional seed gas measurements are necessary. The problem could be sidestepped by using the results from a CFD simulation to calculate the purge mass flow distribution in the annulus (e.g., with particle tracking). Nevertheless, the numerical approach would introduce a different set of uncertainty, modeling and cost issues, which should be carefully evaluated to understand whether computing the purge distribution is more or less convenient than the uniform purge assumption. Another issue is that the calculated uncertainty is relatively high compared to the typical needs of engine manufacturers ($\pm$0.5–1%). This aspect could be improved by optimizing the temperature measurement chain and providing a reliable estimation for the mechanical, windage and heat transfer losses.

Author Contributions: Conceptualization, F.M. and E.G.; methodology, F.M.; software, F.M. and N.K.; validation, F.M., N.K. and A.H.; formal analysis, F.M. and E.G.; investigation, F.M., N.K. and A.H.; resources, N.K. and A.H.; data curation, F.M.; writing—original draft preparation, F.M.; writing—review and editing, E.G.; visualization, F.M.; supervision, E.G.; project administration, E.G.; funding acquisition, E.G. All authors have read and agreed to the published version of the manuscript.

Funding: The project leading to this application has received funding from the Clean Sky 2 Joint Undertaking under the European Union's Horizon 2020 research and innovation program (grant agreement No. 785313).

Institutional Review Board Statement: Not applicable.

Informed Consent Statement: Not applicable.

Data Availability Statement: Restrictions apply to the availability of the data presented in this study. The data are available on request from the corresponding author with prior authorization from GE Aviation.

Acknowledgments: The authors would like to thank M. Daneri and F. Mangini for their contributions to operating the test facility and GE Aviation for their permission to publish this paper.

Conflicts of Interest: The authors declare no conflict of interest. The funders had no role in the design of this study; in the collection, analyses, or interpretation of data; in the writing of the manuscript; or in the decision to publish the results.

Nomenclature

Abbreviations	
HPT, LPT	high-pressure, low-pressure turbine
TVF	turbine vane frame
PFR	purge flow ratio
FHP	five-hole probe
LE	leading edge
LPV, UPV	lower, upper passage vortex
TLF	tip leakage flow
SV	scraping vortex
PD	purge distribution
UP	uniform purge
UHC, USC	upstream hub/shroud cavity
Symbols	
r, θ	radial, tangential coordinate
A, B, C, D	Plane A, B, C, D
P_T, T_T, h_T	total pressure, temperature, enthalpy
L	axial length
c_P	specific heat capacity at constant pressure
η	efficiency
c	concentration
$\dot{m}$	mass flow
ε	effectiveness
Re	Reynolds number
v, M	absolute velocity, Mach number
ρ, μ	density, dynamic viscosity
s	entropy
Subscripts and Superscripts	
1, 2	HPT stage, LPT stage
k, l	cavity indices
0, ms, s	cavity, mainstream, sample
c, fm	combined, fully mixed
$\bar{}$	average
is, ad	isentropic, adiabatic
vol	volumetric

References

1. Hartsel, J. Prediction of effects of mass-transfer cooling on the blade-row efficiency of turbine airfoils. In Proceedings of the 10th Aerospace Sciences Meeting, San Diego, CA, USA, 17–19 January 1972. [CrossRef]
2. Young, J.B.; Horlock, J.H. Defining the Efficiency of a Cooled Turbine. *J. Turbomach.* **2006**, *128*, 658–667. [CrossRef]

3. Berdanier, R.A. Calculating Cooled Turbine Efficiency with Weighted Cooling Flow Distributions. *J. Turbomach.* **2023**, *145*, 061007. [CrossRef]
4. Ong, J.; Miller, R.J.; Uchida, S. The Effect of Coolant Injection on the Endwall Flow of a High Pressure Turbine. *J. Turbomach.* **2012**, *134*, 051003. [CrossRef]
5. Jenny, P.; Abhari, R.S.; Rose, M.G.; Brettschneider, M.; Engel, K.; Gier, J. Unsteady Rotor Hub Passage Vortex Behavior in the Presence of Purge Flow in an Axial Low Pressure Turbine. *J. Turbomach.* **2013**, *135*, 051022. [CrossRef]
6. Regina, K.; Kalfas, A.I.; Abhari, R.S. Experimental Investigation of Purge Flow Effects on a High Pressure Turbine Stage. *J. Turbomach.* **2014**, *137*, 041006. [CrossRef]
7. Dahlqvist, J.E.; Fridh, J. Experimental flow and performance investigations of cavity purge flows in a high pressure tur-bine stage. In Proceedings of the 11th European Conference on Turbomachinery Fluid Dynamics and Thermodynamics, ETC 2015, Madrid, Spain, 23 March 2015.
8. Zlatinov, M.B.; Tan, C.S.; Montgomery, M.; Islam, T.; Harris, M. Turbine Hub and Shroud Sealing Flow Loss Mechanisms. *J. Turbomach.* **2012**, *134*, 061027. [CrossRef]
9. Merli, F.; Hafizovic, A.; Krajnc, N.; Schien, M.; Peters, A.; Heitmeir, F.; Göttlich, E. Aerodynamic Assessment of Turbine Center Frames and Turbine Vane Frames Under the Influence of Purge Flows. In Proceedings of the ASME Turbo Expo 2022: Turbomachinery Technical Conference and Exposition, Rotterdam, The Netherlands, 13–17 June 2022. [CrossRef]
10. Merli, F.; Krajnc, N.; Hafizovic, A.; Göttlich, E. Performance Evaluation in a Fully Purged High-Pressure Turbine Stage Using Seed Gas Concentration Measurements. In Proceedings of the 15th European Turbomachinery Conference, Paper N. ETC2023-268, Budapest, Hungary, 24–28 April 2023; Available online: https://www.euroturbo.eu/publications/conference-proceedings-repository (accessed on 11 June 2023).
11. Neumayer, F.; Kulhanek, G.; Pirker, H.-P.; Jericha, H.; Seyr, A.; Sanz, W. Operational Behavior of a Complex Transonic Test Turbine Facility. In Proceedings of the ASME Turbo Expo 2001: Power for Land, Sea, and Air, New Orleans, LA, USA, 4–7 June 2001. ASME Paper No. GT2000-489. [CrossRef]
12. Hubinka, J.; Santner, C.; Paradiso, B.; Malzacher, F.; Göttlich, E.; Heitmeir, F. Design and construction of a two shaft test turbine for investigation of mid turbine frame flows. In Proceedings of the ISABE, Montreal, QC, Canada, 7–11 September 2009; pp. 7–11.
13. Steiner, M.; Zerobin, S.; Bauinger, S.; Heitmeir, F.; Göttlich, E. Development and Commissioning of A Purge Flow System in A Two Spool Test Facility. In Proceedings of the 12th European Conference on Turbomachinery Fluid dynamics & Thermodynamics, Stockholm, Sweden, 3–7 April 2017. ETC Paper No. ETC2017-115. [CrossRef]
14. Patinios, M.; Merli, F.; Hafizovic, A.; Göttlich, E. The Interaction of Purge Flows with Secondary Flow Features in Turbine Center Frames. In Proceedings of the ASME Turbo Expo 2021: Turbomachinery Technical Conference and Exposition, Online, 7–11 June 2021. [CrossRef]
15. Merli, F.; Hafizovic, A.; Krajnc, N.; Schien, M.; Peters, A.; Heitmeir, F.; Göttlich, E. The Interaction of Main Stream Flow and Cavity Flows in Turbine Center Frames and Turbine Vane Frames. *J. Eng. Gas Turbines Power* **2022**, *145*, 021027. [CrossRef]
16. Bell, I.H.; Wronski, J.; Quoilin, S.; Lemort, V. Pure and Pseudo-pure Fluid Thermophysical Property Evaluation and the Open-Source Thermophysical Property Library CoolProp. *Ind. Eng. Chem. Res.* **2014**, *53*, 2498–2508. [CrossRef] [PubMed]
17. Holman, J.P. *Experimental Methods for Engineers*, 7th ed.; International ed.; McGraw-Hill: New York, NY, USA, 2001.
18. De´nos, R.; Paniagua, G.; Yasa, T.; Fortugno, E. Determination of the Efficiency of a Cooled HP Turbine in a Compression Tube Facility. In Proceedings of the ASME Turbo Expo 2006: Power for Land, Sea, and Air, Barcelona, Spain, 8–11 May 2006; pp. 607–618. [CrossRef]
19. Sterzinger, P.Z.; Zerobin, S.; Merli, F.; Wiesinger, L.; Peters, A.; Maini, G.; Dellacasagrande, M.; Heitmeir, F.; Göttlich, E. Impact of Varying High- and Low-Pressure Turbine Purge Flows on a Turbine Center Frame and Low-Pressure Turbine System. *J. Turbomach.* **2020**, *142*, 101011. [CrossRef]
20. Zerobin, S.; Peters, A.; Bauinger, S.; Ramesh, A.B.; Steiner, M.; Heitmeir, F.; Goettlich, E. Aerodynamic Performance of Turbine Center Frames With Purge Flows—Part I: The Influence of Turbine Purge Flow Rates. *J. Turbomach.* **2018**, *140*, 061009. [CrossRef]